Mechanical actuation of graphene sheets via optically induced forces

Mohammad Mahdi Salary, Sandeep Inampudi, Kuan Zhang, Ellad B. Tadmor, and Hossein Mosallaei

Mechanical Actuation of Graphene Sheets via Optically Induced Forces

Mohammad Mahdi Salary[1], Sandeep Inampudi[1], Kuan Zhang[2], Ellad B. Tadmor[2], Hossein Mosallaei[1*]

[1]*Electrical and Computer Engineering Department, Northeastern University, Boston, MA 02115, USA*

[2]*Department of Aerospace Engineering and Mechanics, The University of Minnesota, Minneapolis, MN 55455, USA*

In this paper, we theoretically demonstrate the strong mechanical response of graphene sheets actuated by near-field optical forces. We study single layer graphene and a two-layer graphene stack with large separation and show that tunable attractive and repulsive forces can be generated. A large nonlinear mechanical response can be obtained by driving the sheets through external radiation and guided modes. We report formation of graphene bubbles of several nanometers in height. Our study points towards new routes for mechanical actuation of graphene providing new platforms for straintronics and flexible optoelectronics.

I. INTRODUCTION

Graphene sheets offer a unique platform for mechanics due to their very low mass density $(1.5 - 2 \text{ g/cm}^3)$, high elastic strength (~ 130 GPa) [1], exceptionally stiff in-plane Young's modulus (~ 1 TPa) [2], strong adhesion, and flexibility [3-5]. These properties have motivated the adoption of graphene in the next generation of nano-mechanical devices. Mechanical actuation of graphene has been demonstrated by applying pressure using gas cavities [6, 7], electric potential [8, 9], thermal expansion [10, 11], acoustic waves [12], electrostatic interactions [13], and electron pumping [14, 15]. Considerable progress has been made to exploit the mechanical properties of graphene for high-sensitivity force/mass detectors [16] and tunable mechanical oscillators [17, 18]. In addition, several interesting physical phenomena induced by strain have been demonstrated [19-23]. It has been shown that the electronic properties of graphene can be engineered by inducing mechanical deformations, which has led to the advent of the field of "straintronics" [24-26].

Recently, optical forces have gained in popularity due to their noncontact nature and ability to manipulate and trap microscopic objects [27-29]. Using optical forces to mechanically actuate graphene holds promise for novel applications in optomechanics [30], such as all-optically tunable filters, switches, and modulators. However, optical forces are notoriously weak, and hence it is necessary to explore possible routes for enhancing these forces for practical applications.

Although a graphene sheet is optically quasi-transparent over the infrared and visible ranges, it interacts strongly with transverse magnetic (TM) light at THz and mid-IR frequencies [31]. This interaction is dominated by interband and intraband transitions of the free carriers in graphene and is highly dispersive [32, 33]. The collective oscillations of the free carriers can produce surface plasmon polaritons (SPPs), enabling significant confinement of light to dimensions much smaller than the free space wavelength. This offers a route for generating strong optical forces on graphene sheets.

The use of SPP-enhanced optical forces in graphene systems can lead to a better performance in terms of attraction and repulsion compared to conventional metal and dielectric systems [34-39] due to higher confinement of SPPs to the surface and lower loss [33]. Further, moving from a three-dimensional structure to a two-dimensional sheet is expected to magnify the effect of the force in terms of the resulting deformation and accelerations. These differences and the unique feature of graphene in terms of electrochemical tunability makes it a promising candidate for optomechanical applications. In this paper, we provide a detailed analysis of the forces generated by SPPs in a single-layer and a two-layer stack of graphene sheets. The calculation of the optical fields is carried out by a general analytic formalism based on the scattering matrix approach for stacked layers of graphene [40]. Once the fields are obtained, we calculate the time-averaged optical force per unit area of the sheets by evaluating the flux of the Maxwell stress tensor (MST) [41]. We show that tunable attraction and repulsion can be achieved for graphene sheets. The nonlinear mechanical signatures are obtained by driving the sheets through external radiation and guided modes. The deformation of the sheets was studied using a nonlinear von Kármán plate theory using both an axisymmetric solution [42] and a subdivision finite element method within a quasicontinuum framework [43, 44]. The paper is organized as follows. In Sec. II, we establish the formulation and introduce the methods used in this work. We investigate the optically induced forces and the mechanical response of a free standing graphene sheet through external excitation in section III. Section IV, illustrates the optically induced forces between two layers of graphene sheets excited by external radiation as well as injection pf guided modes. Finally, the conclusion is drawn in section V.

II. METHODS

A. Scattering Matrix Approach

Consider stacked layers of graphene sheets with the surface conductivity of σ_l separated by dielectric layers with the relative permittivities of ε_l illuminated by transverse magnetic TM plane waves as shown in Fig. 1(a). The total electric and magnetic field components associated with each layer, represented as $\vec{E}_l$ and $\vec{H}_l$, can be formulated as integrals of plane wave modal components propagating in the forward (+z) and backward (-z) direction [40]:

$$\vec{E}_l = \int_{-\infty}^{\infty} \int_{-\infty}^{\infty} \left[a^{(l)+} \vec{\mathscr{E}}^{(l)+} \Phi^{(l)+} + a^{(l)-} \vec{\mathscr{E}}^{(l)-} \Phi^{(l)-} \right] dk_x dk_y \tag{1}$$

$$\vec{H}_l = \int_{-\infty}^{\infty} \int_{-\infty}^{\infty} \left[a^{(l)+} \vec{\mathscr{H}}^{(l)+} \Phi^{(l)+} + a^{(l)-} \vec{\mathscr{E}}^{(l)-} \Phi^{(l)-} \right] dk_x dk_y \tag{2}$$
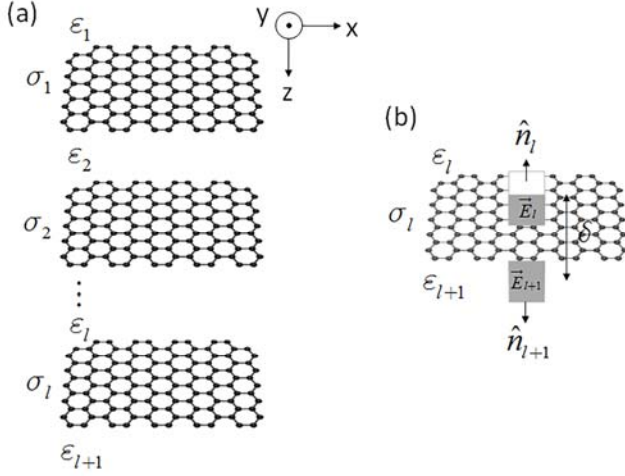

FIG. 1. (a) Schematic representation of stacked layers of graphene sheets separated by dielectric layers. (b) The integration path chosen to calculate force per unit area on a graphene sheet using Maxwell stress tensor method.

Each plane wave component is characterized by transverse wave vector components $\{k_x, k_y\}$ that are conserved in each layer. The quantities $a^{(l)\pm}$ are the unknowns to calculate, representing amplitudes of the plane waves propagating in l-th layer; $\vec{\mathscr{E}}^{(l)\pm}$ and $\vec{\mathscr{H}}^{(l)\pm}$ represent electric and magnetic field modal profiles, respectively, of each plane wave in the l-th layer; and $\Phi^{(l)\pm} = \exp\left(ik_x x + ik_y y \pm ik_z^{(l)} z\right)$ represent the phase factors of plane waves in the l-th layer. In all the above quantities, (+) sign represents the waves travelling in the forward direction and (−) sign represents the waves travelling in the backward direction. The modal field profiles of each layer can be expressed analytically as:

$$\vec{\mathscr{E}}_p^{(l)\pm} = \left\{ \mp \frac{k_z^{(l)} k_x}{\varepsilon_{(l)}}, \mp \frac{k_z^{(l)} k_y}{\varepsilon_{(l)}}, \frac{k_\rho^2}{\varepsilon_{(l)}} \right\} / k_0 k_\rho \tag{3}$$

$$\vec{\mathscr{H}}_p^{(l)\pm} = \left\{ k_y, -k_x, 0 \right\} / k_\rho \tag{4}$$

where $k_0 = \omega / c$, $k_\rho = \sqrt{k_x^2 + k_y^2}$ and $k_z^{(l)} = \sqrt{k_0^2 \varepsilon_{(l)} - (k_x^2 + k_y^2)}$.

Applying the boundary conditions, the scattering matrix equation of the l-th interface can be written as:

$$\begin{bmatrix} a^{(l)-} \\ a^{(l+1)+} \end{bmatrix} = \begin{bmatrix} \Phi^{(l)+} & 0 \\ 0 & \Phi^{(l+1)-} \end{bmatrix} \begin{bmatrix} r^{(l)+} & t^{(l)-} \\ t^{(l)+} & r^{(l)-} \end{bmatrix}$$
$$\begin{bmatrix} \Phi^{(l)+} & 0 \\ 0 & \Phi^{(l+1)-} \end{bmatrix} \begin{bmatrix} a^{(l)+} \\ a^{(l+1)-} \end{bmatrix} \tag{5}$$

where $\Phi^{(l)\pm}$ are calculated at $z = z_l$ and each term in the matrix can be calculated as:

$$r^{(l)+} = \frac{k_z^{(l)} \varepsilon_{(l+1)} - k_z^{(l+1)} \varepsilon_{(l)} + k_z^{(l)} k_z^{(l+1)} \sigma_{(l)} \eta_0}{D} \tag{6}$$

$$r^{(l)-} = \frac{k_z^{(l+1)} \varepsilon_{(l)} - k_z^{(l)} \varepsilon_{(l+1)} + k_z^{(l)} k_z^{(l+1)} \sigma_{(l)} \eta_0}{D} \tag{7}$$

$$t^{(l)+} = \frac{2 k_z^{(l)} \varepsilon_{(l+1)}}{D} \tag{8}$$

$$t^{(l)-} = \frac{2 k_z^{(l+1)} \varepsilon_{(l)}}{D} \tag{9}$$

where η_0 is the wave impedance of free-space and

$$D = k_z^{(l)} \varepsilon_{(l+1)} + k_z^{(l+1)} \varepsilon_{(l)} + k_z^{(l)} k_z^{(l+1)} \sigma_{(l)} \eta_0 \tag{10}$$

The eigen modes (or guided modes) of the system of layers, characterized by the tangential wavevector component k_ρ for each polarization, can be identified as the poles of the total reflection coefficient matrix. For a simple system, with a 2D sheet separating two semi-infinite uniaxial media, the poles can be directly identified as the zeros of the denominator D given in (10). In case of a 3-layer system with two 2D sheets separated by a finite layer, according to the recursive reflection formulae, the condition for guiding a wave is [40]:

$$1 - \Phi^{(l)-} r^{(l-1)-} \Phi^{(l)-} \Phi^{(l)+} r^{(l)+} \Phi^{(l)+} = 0 \tag{11}$$

B. Maxwell Stress Tensor Method

Once the fields are obtained, the time-averaged optical force at each interface is calculated by evaluating the flux of the Maxwell stress tensor (MST) as [41]:

$$\vec{F}_l = -\frac{1}{2} \text{Re} \left\{ \oiint_{S_l} dS \left[\hat{n} . \overline{\overline{T}}(\vec{r}) \right] \right\} \tag{12}$$

where S_l is the integration path enclosing the surface of l-th graphene sheet. The complex Maxwell stress tensor is defined in terms of electromagnetic fields as:

$$\overline{\overline{T}}(\vec{r}) = \frac{1}{2}\left(\overline{D}.\overline{E}^* + \overline{B}^*.\overline{H}\right)\overline{\overline{I}} - \overline{D}\overline{E}^* - \overline{B}^*\overline{H} \qquad (13)$$

where $\overline{\overline{I}}$ is the 3×3 identity matrix and an asterisk (∗) denotes the complex conjugate. By choosing the integration path around the infinitesimal segments of the graphene sheet as shown in Fig. 1(b), we are able to calculate the force per unit area in terms of the fields above and below the sheet as:

$$\vec{F}_l = \frac{1}{2}\text{Re}\left\{\hat{z}.\overline{\overline{T}}(z = z_l^-) - \hat{z}.\overline{\overline{T}}(z = z_l^+)\right\} \qquad (14)$$

where:

$$\hat{z}.\overline{\overline{T}}(z = z_l^+) = \hat{z}\left[\frac{\varepsilon_{l+1}}{2}\left(\left|E_x(z = z_l^+)\right|^2 + \left|E_y(z = z_l^+)\right|^2 - \left|E_z(z = z_l^+)\right|^2\right)\right.$$
$$-\frac{\mu_{l+1}}{2}\left(\left|H_x(z = z_l^+)\right|^2 + \left|H_y(z = z_l^+)\right|^2 - \left|H_z(z = z_l^+)\right|^2\right)\bigg]$$
$$+\hat{x}\left[-\varepsilon_{l+1}E_z(z = z_l^+)E_x^*(z = z_l^+) - \mu_{l+1}H_z(z = z_l^+)H_x^*(z = z_l^+)\right]$$
$$+\hat{y}\left[-\varepsilon_{l+1}E_z(z = z_l^+)E_y^*(z = z_l^+) - \mu_{l+1}H_z(z = z_l^+)H_y^*(z = z_l^+)\right]$$
$$(15)$$

and

$$\hat{z}.\overline{\overline{T}}(z = z_l^-) = \hat{z}\left[\frac{\varepsilon_l}{2}\left(\left|E_x(z = z_l^-)\right|^2 + \left|E_y(z = z_l^-)\right|^2 - \left|E_z(z = z_l^-)\right|^2\right)\right.$$
$$-\frac{\mu_l}{2}\left(\left|H_x(z = z_l^-)\right|^2 + \left|H_y(z = z_l^-)\right|^2 - \left|H_z(z = z_l^-)\right|^2\right)\bigg]$$
$$+\hat{x}\left[-\varepsilon_l E_z(z = z_l^-)E_x^*(z = z_l^-) - \mu_l H_z(z = z_l^-)H_x^*(z = z_l^-)\right]$$
$$+\hat{y}\left[-\varepsilon_l E_z(z = z_l^-)E_y^*(z = z_l^-) - \mu_l H_z(z = z_l^-)H_y^*(z = z_l^-)\right]$$
$$(16)$$

Evidently, the transverse components of the optical force on the infinitesimal segment of the sheet is zero. With knowledge of the fields above and below the sheet we arrive at the closed-form force per unit area on the sheet.

C. Nonlinear von Kármán plate theory

In the continuum mechanics framework, the mechanical behavior of a graphene sheet can be described by mapping a two-dimensional plane to three-dimensional space. In this case, in-plane stretch is quantified by 2D Green-Lagrange Strain Tensor and bending is described by a curvature tensor, both defined with respect to the ground state of a flat graphene sheet. Under the assumption of relatively small deformation but with moderately large deflection, a set of nonlinear equations can be used to describe the mechanical behavior of graphene sheet which closely resemble the von Karman equations for an isotropic elastic thin plate [42].

In the case of a circular graphene sheet subjected to axisymmetric loading $q(r)$, the in-plane displacements and the lateral deflection expressed in polar coordinates are $u_r = u(r)$, $u_\theta = 0$, and $w = w(r)$, respectively where $r = \sqrt{x^2 + y^2}$. The equilibrium equations in terms of displacements can be written as [42]

$$\frac{d^2u}{dr^2} + \frac{1}{r}\frac{du}{dr} - \frac{u}{r^2} = -\frac{1-v}{2r}\left(\frac{dw}{dr}\right)^2 - \frac{dw}{dr}\frac{d^2w}{dr^2} \qquad (17)$$

$$D\left(\frac{d^3w}{dr^3} + \frac{1}{r}\frac{d^2w}{dr^2} - \frac{1}{r^2}\frac{dw}{dr}\right) - \frac{E_{2D}}{1-v^2}\frac{dw}{dr}\left(\frac{du}{dr} + v\frac{u}{r} + \frac{1}{2}\left(\frac{dw}{dr}\right)^2\right)$$
$$= \frac{1}{r}\int_0^r qr\,dr$$
$$(18)$$

where E_{2D}, v, and D are the 2D Young's Modulus, Poisson's ration, and bending moduli, respectively. A finite difference approach is used to solve equations (17) and (18) subject to axisymmetric pressure distribution obtained from the electromagnetic solution with zero displacements imposed at the sheet edge at $r = a$.

As a more general solution methodology, we have also a nonlinear subdivision finite element method implemented within a quasicontinuum framework [43, 44]. In this approach, the internal energy is calculated using a hyperelastic potential that depends on the in-plane right Cauchy-Green deformation tensor **C**, and the curvature tensor **K**. For these calculations we adopt a linearized model about the planar ground state of graphene. The problem is solved quasistatically using subdivision finite elements [44], which provide a smooth parametrization with square integrable curvature. At each strain increment, we obtain stable equilibrium configurations by numerical minimization using a conjugate gradient method.

An approximate solution for graphene bubbles can also be obtained to estimate the center deflection [45]. Due to the nonuniform distribution of the pressure arising from external excitations, the deflection profile is relatively localized towards the center. We assume a deflection profile in form of:

$$w = h\left(1 - \frac{r^2}{a^2}\right)\sum_n C_n\left(1 - \frac{\rho^2}{a^2}\right)^n. \qquad (19)$$

The in-plane strain energy and the bending energy are modeled using a von Kármán plate theory [44]. A variational approach is adopted whereby the approximate equilibrium solution is obtained by minimizing the total energy with respect to the unknown coefficients in (19).

In all the models, the graphene sheet is taken to be transversely isotropic with linear elastic properties $E_{2D} = 336\,\text{N/m}$, $v = 0.165$, and $D = 0.238\,\text{nN}\cdot\text{nm}$ consistent with experimental and *ab initio* calculations [42].

It should be remarked that for the investigation of the optomechanical response of a graphene sheets coupled analysis of the fields and deformation kinematics should be carried out since the optical forces change as the graphene sheet bends. The study requires a multi-scale approach as the locally induced strains can change the electronic structure of graphene and affect the conductivity. However, for small deformations the change in the conductivity is

negligible. Moreover, the coupling between electromagnetic and mechanical equations is weak and they can be decoupled to give an approximate solution. Throughout this work, we restrict ourselves to this weak-coupling regime to show the proof of concept. The implications of this approximation are studied and provided in the supplemental material.

III. OPTICAL FORCES ON A FREE-STANDING GRAPHENE SHEET

We start by considering a free-standing graphene layer. To highlight the similarities and differences between graphene and metallic films, a free-standing gold thin film with a thickness of 10nm is considered for comparison. The near-field excitation accesses surface plasmons, which leads to ultrahigh optical forces. The key feature in this process is the strong enhancement of evanescent waves. To demonstrate this effect, a graphene sheet and a gold thin film are excited by a TM polarized light from above with a wavelength λ as depicted in the insets of Fig. 2. Referring to the coordinate system of Fig. 2, we express the electric field as $\vec{E} = E_0 \exp{(ik_i.r - i\omega t)}\widehat{k_i}$, where $\overrightarrow{k_i} = k_\rho\hat{\rho} + k_z\hat{z}$ is the wavevector, and $k_\rho^2 + k_z^2 = k_0^2$ with $k_0 = 2\pi/\lambda$ and $k_\rho = \sqrt{k_x^2 + k_y^2}$. In the following, the gold thin film is studied in the visible spectrum with experimentally determined values for permittivity [46], and the graphene is considered in the THz and mid-IR frequencies with experimentally determined conductivity fitted to a Drude model [47] for a surface carrier density of $n_s = 7.37 \times 10^{16}\text{m}^{-2}$ and scattering time of $\tau = 500fs$.

Figures 2a and 2b represent the wavevector resolved reflection coefficients of a graphene sheet and thin metal layer, respectively, demonstrating SPP resonance (at the poles as $R \to \infty$). In case of a free standing graphene sheet the wavevector corresponding to SPP resonance can be analytically derived as [32]:

$$k_\rho^{SPP} = k_0\sqrt{\epsilon(1 - 4\epsilon/\sigma^2\eta_0^2)}, \tag{20}$$

where ϵ is the relative permittivity of the medium and σ is the surface conductivity of the sheet. The metal layer due to its finite thickness normally supports two SPP modes with symmetric and anti-symmetric field profiles. However, due to the extremely small thickness considered in this example, the resonance condition for the asymmetric mode approaches infinity and is no longer accessible [48].

The compressive optical force per unit area (pressure) is linearly proportional to the incident optical power density $P = |E_0|^2/\eta$, where η is the free space impedance and E_0 is the amplitude of the incident field. Figures 2c and 2d show the optical pressure on the graphene sheet and gold thin film, respectively, for an optical power density of $1\text{kW}/\text{cm}^2$. As can be observed, the pressure is dominated by two opposite peaks close to the SPP resonance. The switching of the force from positive to negative is a result of the rapid variation of the scattering phase shift across the resonance.

Crossing the resonance, the reflection and transmission pick up a phase shift equal to π.

Our results show that the SPP-induced force on a free standing graphene sheet is significantly larger than on a gold thin film (by 3 orders of magnitude). We attribute this to the higher confinement of SPPs to the surface [33]. Moreover, the lower loss of graphene compared to gold provides propagation over a larger distance which translate into larger deflections for similarly sized structures. It is also noteworthy to mention that in practice creating a very thin homogeneous metal layer faces fabrication difficulties while free-standing graphene monolayers can be prepared by mechanical exfoliation of graphite.
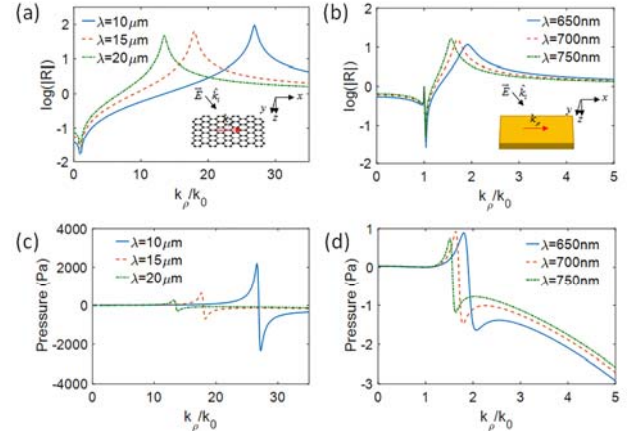

FIG. 2. (a) and (b) show the reflection of graphene and gold as a function of the transverse component of wavevector k_ρ. The insets show sketches of a graphene sheet and gold thin film excited by a TM evanescent light. (c) and (d) show the optical pressure on the graphene sheet and the gold thin film versus k_ρ at different wavelengths.

In order to demonstrate the mechanical interaction of the graphene sheet with light, we use an external point source to excite SPPs on the graphene surface. This can be done in practice by nearfield coupling with a sharpened metallic tip or tapering metal aperture above the sheet, which can be modeled as a dipole source with moment $\vec{p} = p_x\hat{x} + p_y\hat{y} + p_z\hat{z}$. Here, we consider a vertically-oriented dipole with dipole moment $\vec{p} = p_z\hat{z}$ placed 50nm above the graphene surface for excitation of surface plasmons. The field profile of the dipole can be expressed as a spectrum of TM plane waves with the amplitudes at the graphene surface given by $a = (p_z k_\rho/k_z)\exp{(ik_z h)}$, where h is the height of dipole above the sheet [40, 49].

The part of the spectrum with $k_\rho > k_0$ is associated with the dipole's evanescent field. Evidently, the smaller k_ρ, the more field survives across the distance h to significantly couple to the graphene sheet. As k_ρ increases, the field reaching the surface no longer couples to the sheet above a critical cut-off wavevector [50]. The excitation of evanescent fields by the dipole source at the graphene surface and the subsequent stimulation of wavevector resolved forces results in a non-zero net pressure on the

sheet. Moreover, as implied by the results in Fig. 2 and shown further below, the wavelength of the optical excitation can be controlled to yield tunable optomechanical effects, even switching the sign of the force from attractive to repulsive by shifting the SPP resonance with respect to the cut-off wavevector.

As an explicit example, we study a circular graphene sheet with the radius of $R = 1\mu m$. The optical pressure is obtained by using the MST method and is linearly proportional to the optical power of the source, $P_{rad} = (c_0 k_0^4 / 12\pi\epsilon_0)|p|^2$, with c_0 being the speed of light in a vacuum. Here, the results are calculated for a source with a radiated power of 1.5mW. Figure 3a shows the distributed transverse optical pressure across the sheet for $\lambda = 8\mu m$ corresponding to the SPP wavelength of $\lambda_{SPP} = 238.2nm$. The pressure is dominated by a negative peak, which translates to attraction towards the dipole source. The resulting deformation profile across the graphene sheet is calculated using a nonlinear plate theory and is shown in Fig. 3b. As can be seen, a blister with radius of 1μm and height of 2nm is formed. The magnitude of the deflection depends on the pressure and blister radius. One can expect larger deflections for higher input power and larger radius of the sheet. According to Fig. 3c, as the wavelength decreases, the SPP resonance shifts to larger k_ρ shifting the attractive forces above the cut-off in the dipole excitation spectrum leading to the domination of repulsive forces. To demonstrate this effect, the results for the pressure distribution and the induced deformation at $\lambda = 5\mu m$ are presented in Figs. 3c and 2d, respectively. The corresponding SPP wavelength in this case is $\lambda_{SPP} = 93.1nm$. The pressure dip in the center is a result of attraction toward the source, while the overall interaction is dominated by repulsive forces forming a graphene bubble with a height of about 1nm. Figure 3e compares the results of the axisymmetric, quasicontinuum and the approximate solutions, which are found to be in good agreement. (The main differences between the methods are the mesh resolution and imposed boundary conditions.) Such nanoscale mechanical responses can be captured in practice through direct imaging of the spatial shape using scanning force microscopy (SFM) [51], transmission electron microscopy (TEM) [52], or Raman spectroscopy with optical probes [53].

As implied by the results, if the SPP resonance is moved beyond the cut-off wavevector and becomes inaccessible by the dipole excitation spectrum, we will observe repulsion phenomenon. However, it should be remarked that suppressing the plasmon resonance will drastically diminish the optically induced forces and leads to no appreciable deformation. This can be clearly seen from the smaller forces and deformations at $\lambda = 5\mu m$ comparing to those at $\lambda = 8\mu m$.
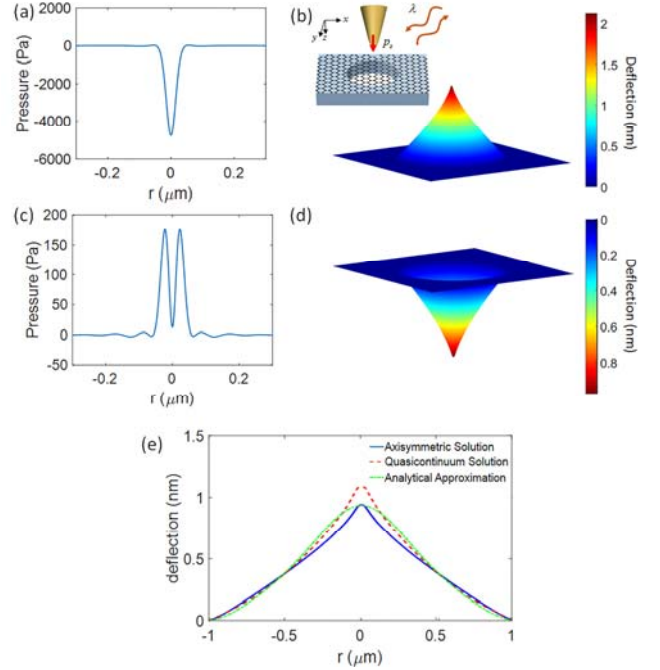

FIG. 3. (a) and (b) show the pressure distribution and deflection of a graphene sheet resulting from excitation by a vertically oriented dipole source of $\lambda = 8\mu m$ with a radiated power of 1.5mW placed 50nm above the sheet. The SPP wavelength is $\lambda_{SPP} = 238.2nm$. The inset shows a schematic of a circular graphene sheet with a radius of 1μm excited by scattering from an AFM tip modeled with a vertical dipole depicted as the red arrow. (c) and (d) show the results at lower wavelength of $\lambda = 5\mu m$ which leads to repulsion phenomenon. The SPP wavelength is $\lambda_{SPP} = 93.1nm$. (e) compares the deflection predicted by the axisymmetric, quasicontinuum and approximate solutions for the nonlinear von Kármán plate theory.

IV. OPTICALLY INDUCED FORCES BETWEEN TWO LAYERS OF GRAPHENE SHEETS

Next we consider a stack of two graphene layers separated by a distance d. (Note that d is much larger than the equilibrium separation distance between graphene layers, so this is not a graphene bilayer.) In this case, the mutual interaction of degenerate resonances or guided modes induces a splitting into symmetric and asymmetric modes. This is analogous to the well-known states formed in Insulator-Metal-Insulator (IMI) or Metal-Insulator-Metal (MIM) structures [36, 37]. Using the convention used in the metallic systems, symmetric modes refer to modes of even vector parity (E_x is even, E_z and H_y are odd functions of z) and the asymmetric modes refer to mode of odd vector parity (E_x is odd, E_z and H_y are even functions of z). In this coupled system, we demonstrate that these modes are characterized by attractive and repulsive optical force between the sheets.

There are two ways to excite coupled resonances on the graphene sheets depending on whether the incident power comes in the form of external radiation or a guided mode. First, we consider the case of external radiation. For a single

source of radiation above the two layers, the force on the sheets will not be equal. In order to characterize the guided modes of the system, we plot the wavevector-resolved reflection of TM excitation in Fig. 4a for a two-layer graphene stack with a separation distance of $d = 100$nm at $\lambda = 10$μm. Two resonances are observed, corresponding to the symmetric and asymmetric modes, with the field profiles of transverse electric field E_x shown in the inset of the figure. The optical pressure on the top sheet as a function of k_ρ obtained for a normalized power density of 1kW/cm^2 is plotted in Fig. 4b. The pressure is dominated by two large peaks of opposite sign at the two resonances. Referring to the coordinates in the inset of Fig. 4b, a positive pressure for the asymmetric mode indicates an attractive force between the sheets and a negative pressure for the symmetric mode corresponds to a repulsive force between the sheets. The pressure on the bottom sheet has the opposite sign and is not plotted.

In order to show the dependence of the optical pressure on the distance between the layers, in Fig. 4c we plot the pressure as a function of k_ρ and separation distance d at $\lambda = 10$μm. As the distance between the sheets increases, the pressure decreases exponentially and the two guided modes approach degeneracy. In this limit, the modes are decoupled and merge so that the pressure behavior is similar to that of a single graphene layer with the force flipping from negative to positive across resonance. The effect of the incident wavelength in the wavevector spectra of pressure is also presented in Fig. 4d for a separation distance of $d = \lambda/100$ between the sheets. As can be seen, both the repulsive and attractive pressures decrease in magnitude as the wavelength increases.

Next, we consider a vertical dipole source with a radiated power of 1.5mW placed 50nm above the top sheet. At small separations, the sheets are well-coupled and the attractive force between the sheets is the dominant force as it occurs further form the cut-off wavevector compared to the repulsive force and is more strongly excited by the dipole source. The results for the pressure distribution across both sheets and their deformation profiles are shown in Figs. 4e and 3f, respectively, for $\lambda = 5$μm and $d = 10$nm. At large separations, the sheets get decoupled and will have degenerate resonances. As a result, both sheets will be attracted (or repulsed) by the source similar to a single graphene layer. To demonstrate this effect, the pressure distributions and deflections for $\lambda = 5$μm and $d = 40$nm are shown in Figs. 4g and 4h, respectively.

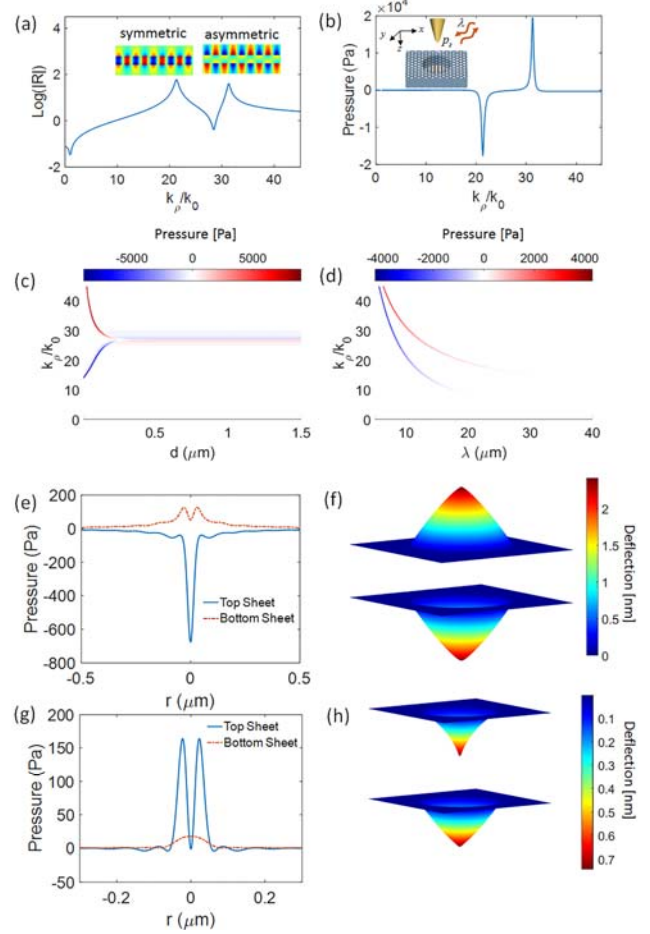FIG. 4 (a) The reflection versus k_ρ from a two-layer graphene stack with a separation distance $d = 100$nm for $\lambda = 10$μm. The field profiles of transverse electric field are plotted in the inset. (b) The optical pressure on the top graphene sheet. (c) The pressure versus k_ρ and normalized separation distance for $\lambda = 10$μm. (d) The pressure versus k_x and incident wavelength for $d = \lambda/100$. (e) and (f) show the pressure distribution and the deformation of the graphene sheets for $d = 10$nm excited by a vertical dipole source with radiate power of 1.5mW at $\lambda = 5$μm. (g) and (h): same as above for a separation distance of $d = 40$nm.

The second technique for excitation is to inject light from the side, activating guided modes that propagate along the sheets and interact evanescently. In this case, the force on both sheets will be equal and as the separation between the layers increases the force tends to zero. The evanescent mode can be excited by diffraction from a grating, coupling to a prism, or another waveguide. This excitation scheme offers the opportunity to selectively couple to one of the asymmetric or symmetric modes to obtain a repulsive or attractive force making it possible to tune the deflection from positive to negative. This property is of interest in particular for realizing optically-controlled nanoactuators. In order to excite the guided modes in the coupled system of two graphene layers we have used mode-matching technique in combination with the scattering matrix approach [54, 55]. These fields have a TM profile. Referring

to the coordinate system in Fig. 5, one can express the fields as $\vec{E} = E_x\hat{x} + E_z\hat{z}$ and $\vec{H} = H_y\hat{y}$. The optical pressure is linearly proportional to the power flowing along the propagation direction, which can be obtained per unit width of the sheets as:

$$= \frac{P_z}{W} = \frac{1}{2}\text{Re}\left\{\int_{-\infty}^{+\infty} \vec{E} \times \vec{H}^* dz\right\} = \text{Re}\left\{\frac{k_z}{\omega\varepsilon_0}\right\}\int_0^{+\infty}|H_y|^2 dz.$$

(21)

The optical power per unit width distributed along the sheets is assumed to be 1mW/μm. The dependence of the attractive and repulsive pressure on the excitation wavelength and the distance between the sheets is shown in Figs. 5a and 5b, respectively. Two coupling regimes are observed in Figs. 5a and 5b. For large separation distances, the optical pressures in the antisymmetric and symmetric modes have nearly equivalent magnitudes; at small separations, the asymmetric mode produces a significantly enhanced pressure compared to the symmetric counterpart. In the latter regime, the magnitude of the attractive pressure for the asymmetric mode shows an exponential dependence on separation distance, whereas the repulsive pressure for the symmetric mode is only weakly related to separation. The physical explanation for this difference can be obtained by observing that the asymmetric mode is strongly confined between the two sheets. A similar behavior is reported [36] for the attractive and repulsive optical pressures between two metallic films. However, the magnitude of optical pressures in the coupled graphene system is more than two orders of magnitude larger than for the metallic structures.

Figures 5c and 5d show the deformation resulting from symmetric and asymmetric modes for two graphene sheets of length 2μm and an infinitely long width with open ends for $\lambda = 10$μm and $d = 200$nm. The asymmetry in the shape profile of deformation is a result of loss on SPP propagation.
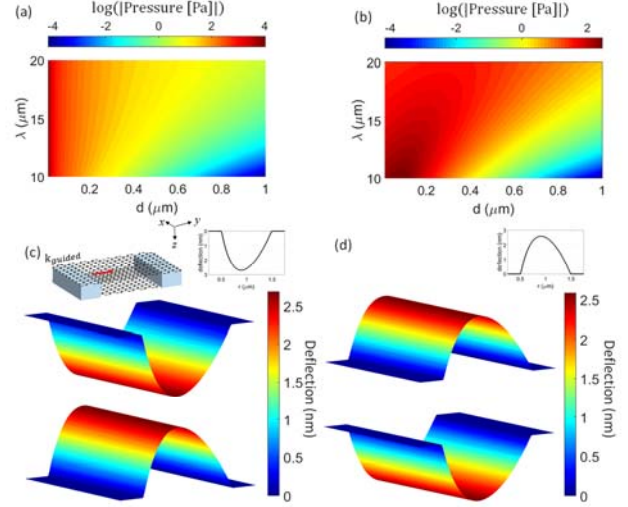

FIG. 5. (a) and (b) show the dependence of the magnitude of the attractive and repulsive pressures between the sheets on the separation distance and incident wavelength, respectively. (c) and (d) show the deformation of the sheets for the attractive and repulsive modes for a separation distance of 100nm for $\lambda = 10$μm. The deflection profiles across the top sheets are shown in the inset to clarify the asymmetry. The inset in (c) depicts a schematic of two graphene sheets excited by a guided mode injected from the side.

V.   CONCLUSION

In conclusion, we have shown that near-field optical excitations can generate large forces on graphene sheets. The use of evanescently coupled guided resonances strongly enhances the optical forces, which lead to the formation of localized blisters in the graphene sheets. Guided modes in graphene structures enable a rich set of phenomena and can add new dimensions to straintronics and flexible optoelectronics. There are many degrees of freedom and possibilities to explore due to the presence of both attractive and repulsive resonances. The ability to tailor guided resonances offers exciting opportunities for tailoring complex force patterns that could be used for applications such as compensation for Casimir forces to avoid stiction in nanoelectromechanical devices, flattening wrinkles in the deposition process of graphene, and the generation of engineered deformation patterns in graphene. Guided resonances can also be exploited to design integrated, all-optical, tunable optomechanical devices.

*hosseinm@ece.neu.edu

[1] H. Roy, C. V. Kallinger, B. Marsen, and K. Sattler, J. Appl. Phys. 83, 4695 (1998).
[2] C. Lee, X. Wei, J. Kysar and J. Hone, Science 321, 385 (2008).
[3] G. Tsoukleri, J. Parthenios, K. Papagelis, R. Jalil, A. Ferrari, A. Geim, K. Novoselov and C. Galiotis, Small 5, 2397 (2009).
[3] J. W. Jiang, J. S. Wang and B. Li, Phys. Rev. B 80, 113405 (2009).

[4] S. Koenig, N. Boddeti, M. Dunn and J. Bunch, Nature Nanotech 6, 543 (2011).

[5] J. Bunch and M. Dunn, Solid State Communications 152, 1359 (2012).

[6] N. Boddeti, X. Liu, R. Long, J. Xiao, J. Bunch and M. Dunn, Nano Letters 13, 6216 (2013).

[7] J. H. Lee, J. Y. Tan, C. T. Toh, S. P. Koenig, V. E. Fedorov, A. H. Castro Neto and B. Özyilmaz, Nano Letters 14, 2677 (2014).

[8] X. Xie, L. Qu, C. Zhou, Y. Li, J. Zhu, H. Bai, G. Shi and L. Dai, ACS Nano 4, 6050 (2010).

[9] J. Liang, Y. Huang, J. Oh, M. Kozlov, D. Sui, S. Fang, R. Baughman, Y. Ma and Y. Chen, Adv. Funct. Mater. 21, 3778 (2011).

[10] H. Conley, N. Lavrik, D. Prasai and K. Bolotin, Nano Letters 11, 4748 (2011).

[11] S. Zhu, R. Shabani, J. Rho, Y. Kim, B. H. Hong, J. Ahn, and H. J. Cho, Nano Letters 11, 977 (2011).

[12] S. Bae, O. Kahya, B. Sharma, J. Kwon, H. Cho, B. Özyilmaz and J. Ahn, ACS Nano 7, 3130 (2013).

[13] J. Bunch, A. van der Zande, S. Verbridge, I. Frank, D. Tanenbaum, J. Parpia, H. Craighead and P. McEuen, Science 315, (2007).

[14] N. Klimov, S. Jung, S. Zhu, T. Li, C. Wright, S. Solares, D. Newell, N. Zhitenev and J. Stroscio, Science 336, 1557 (2012).

[15] S. Zhu, Y. Huang, N. Klimov, D. Newell, N. Zhitenev, J. Stroscio, S. Solares and T. Li, Phys. Rev. B 90, 075426 (2014).

[16] C. Chen, S. Rosenblatt, K. Bolotin, W. Kalb, P. Kim, I. Kymissis, H. Stormer, T. Heinz and J. Hone, Nature Nanotech 4, 861 (2009).

[17] C. Chen, S. Lee, V. Deshpande, G. Lee, M. Lekas, K. Shepard and J. Hone, Nature Nanotech 8, (2013).

[18] R. A. Barton, I. R. Storch, V. P. Adiga, R. Sakakibara, B. R. Cipriany, B. Ilic, S. P. Wang, P. Ong, P. L. McEuen, J. M. Parpia and H. G. Craighead, Nano Letters 12, 4681 (2012).

[19] V. Pereira, A. Castro Neto and N. Peres, Phys. Rev. B 80, 045401 (2009).

[20] D. Yoon, Y. Son and H. Cheong, Phys. Rev. Lett. 106, 155502 (2011).

[21] C. Si, Z. Liu, W. Duan and F. Liu, Phys. Rev. Lett. 111, 196802 (2013).

[22] N. Levy, S. Burke, K. Meaker, M. Panlasigui, A. Zettl, F. Guinea, A. Neto and M. Crommie, Science 329, 544 (2010).

[23] F. Guinea, M. Katsnelson and A. Geim, Nat Phys 6, 30 (2009).

[24] V. Pereira and A. Castro Neto, Phys. Rev. Lett. 103, 046801 (2009).

[25] G. Naumis and P. Roman-Taboada, Phys. Rev. B 89, 241404(R) (2014).

[26] C. Si, Z. Sun and F. Liu, Nanoscale 8, 3207 (2016).

[27] A. Ashkin and J. Dziedzic, Science 235, 1517 (1987).

[28] H. Ito, T. Nakata, K. Sakaki, M. Ohtsu, K. I. Lee, and W. Jhe, Phys. Rev. Lett. 76, 4500 (1996).

[29] M. Salary and H. Mosallaei, Phys. Rev. B 94, 035410 (2016).

[30] S. Mousavi, P. Rakich and Z. Wang, ACS Photonics 1, 1107 (2014).

[31] K. Mak, M. Sfeir, Y. Wu, C. Lui, J. Misewich and T. Heinz, Phys. Rev. Lett. 101, 196405 (2008).

[32] G. Hanson, J. Appl. Phys. 103, 064302 (2008).

[33] M. Jablan, H. Buljan and M. Soljačić, Phys. Rev. B 80, 245435 (2009).

[34] D. Woolf, M. Loncar and F. Capasso, Opt. Express 17, 19996 (2009).

[35] D. Li, N. Lawandy and R. Zia, Opt. Express 21, 20900 (2013).

[36] Povinelli, M. Lončar, M. Ibanescu, E. Smythe, S. Johnson, F. Capasso and J. Joannopoulos, Optics Letters 30, 3042 (2005).

[37] M. Li, W. Pernice and H. Tang, Nature Photonics 3, 464 (2009).

[38] M. Scullion, Y. Arita, T. Krauss and K. Dholakia, Optica 2, 816 (2015).

[39] A. Rodriguez, A. McCauley, P. Hui, D. Woolf, E. Iwase, F. Capasso, M. Loncar and S. Johnson, Opt. Express 19, 2225 (2011).

[40] S. Inampudi, M. Nazari, A. Forouzmand and H. Mosallaei, J. Appl. Phys. 119, 025301 (2016).

[41] B. Kemp, T. Grzegorczyk and J. Kong, Opt. Express 13, 9280 (2005).

[42] P. Wang, W. Gao, Z. Cao, K. Liechti and R. Huang, Journal of Applied Mechanics 80, 040905 (2013).

[43] E. B. Tadmor, M. Ortiz and R. Phillips, Phil. Mag. A 73, 1529 (1996).

[44] K. Zhang and M. Arroyo, J. Mech. Phys. Solids 72, 61 (2014).

[45] K. Yue, W. Gao, R. Huang and K. Liechti, J. Appl. Phys. 112, 083512 (2012).

[46] P. Johnson and R. Christy, Phys. Rev. B 6, 4370 (1972).

[47] A. Woessner, M. Lundeberg, Y. Gao, A. Principi, P. Alonso-González, M. Carrega, K. Watanabe, T. Taniguchi, G. Vignale, M. Polini, J. Hone, R. Hillenbrand and F. Koppens, Nature Materials 14, (2014).

[48] S. Maier, Plasmonics (Springer, New York, 2007).

[49] A. Nikitin, F. Guinea, F. Garcia-Vidal and L. Martin-Moreno, Phys. Rev. B 84, (2011).

[50] F. Koppens, D. Chang and F. García de Abajo, Nano Letters 11, (2011).

[51] D. Garcia-Sanchez, A. van der Zande, A. Paulo, B. Lassagne, P. McEuen and A. Bachtold, Nano Letters 8, 1399 (2008).

[52] C. Lee, X. Wei, J. Kysar and J. Hone, Science 321, 385 (2008).

[53] A. Reserbat-Plantey, L. Marty, O. Arcizet, N. Bendiab and V. Bouchiat, Nature Nanotech 7, 151 (2012).

[54] S. Thongrattanasiri, J. Elser and V. Podolskiy, Journal of The Optical Society of America B **26**, B102 (2009).

[55] S. Inampudi, I. Smolyaninov and V. Podolskiy, Optics Letters **37**, 2976 (2012).